

A rotational Raman study under non-thermal conditions in a pulsed CO₂ glow discharge

Citation for published version (APA):

Klarenaar, B. L. M., Grofulovi, M., Morillo-Candas, A. S., van den Bekerom, D. C. M., Damen, M. A., van de Sanden, M. C. M., ... Engeln, R. (2018). A rotational Raman study under non-thermal conditions in a pulsed CO₂ glow discharge. *Plasma Sources Science and Technology*, 27(4), [045009]. DOI: 10.1088/1361-6595/aabab6

DOI:

[10.1088/1361-6595/aabab6](https://doi.org/10.1088/1361-6595/aabab6)

Document status and date:

Published: 25/04/2018

Document Version:

Accepted manuscript including changes made at the peer-review stage

Please check the document version of this publication:

- A submitted manuscript is the version of the article upon submission and before peer-review. There can be important differences between the submitted version and the official published version of record. People interested in the research are advised to contact the author for the final version of the publication, or visit the DOI to the publisher's website.
- The final author version and the galley proof are versions of the publication after peer review.
- The final published version features the final layout of the paper including the volume, issue and page numbers.

[Link to publication](#)

General rights

Copyright and moral rights for the publications made accessible in the public portal are retained by the authors and/or other copyright owners and it is a condition of accessing publications that users recognise and abide by the legal requirements associated with these rights.

- Users may download and print one copy of any publication from the public portal for the purpose of private study or research.
- You may not further distribute the material or use it for any profit-making activity or commercial gain
- You may freely distribute the URL identifying the publication in the public portal.

If the publication is distributed under the terms of Article 25fa of the Dutch Copyright Act, indicated by the "Taverne" license above, please follow below link for the End User Agreement:

www.tue.nl/taverne

Take down policy

If you believe that this document breaches copyright please contact us at:

openaccess@tue.nl

providing details and we will investigate your claim.

A rotational Raman study under non-thermal conditions in a pulsed CO₂ glow discharge

B.L.M. Klarenaar¹, M. Grofulović², A.S. Morillo-Candas³, D.C.M. van den Bekerom⁴
M.A. Damen¹, M.C.M. van de Sanden^{1,4}, O. Guaitella³, and R. Engeln¹

¹Department of Applied Physics, Eindhoven University of Technology, 5600 MB Eindhoven, The Netherlands

²Instituto de Plasmas e Fusão Nuclear, Instituto Superior Técnico, Universidade de Lisboa, 1049-001 Lisbon, Portugal

³Laboratoire de Physique des Plasmas, Ecole Polytechnique-CNRS-Univ Paris-Sud-UPMC, 91128 Palaiseau, France

⁴DIFFER - Dutch Institute for Fundamental Energy Research, De Zaal 20, 5612 AJ Eindhoven, The Netherlands

Abstract

The implementation of *in situ* rotational Raman spectroscopy is realized for a pulsed glow discharge in CO₂ in the mbar range and is used to study the rotational temperature and molecular number densities of CO₂, CO, and O₂. The polarizability anisotropy of these molecules is required for extracting number densities from the recorded spectra and is determined for incident photons of 532 nm. The spatiotemporally-resolved measurements are performed in the same reactor and at equal discharge conditions (5–10 ms on-off cycle, 50 mA plasma current, 6.7 mbar pressure) as in recently published work employing *in situ* Fourier transform infrared (FTIR) spectroscopy. The rotational temperature ranges from 394 K to 809 K from start to end of the discharge pulse and is constant over the length of the reactor. The discharge is demonstrated to be spatially uniform in gas composition, with a CO₂ conversion factor of 0.15 ± 0.02 . Rotational temperatures and molecular composition agree well with the FTIR results, while the spatial uniformity confirms the assumption made for the FTIR analysis of a homogeneous medium over the line-of-sight of absorption. Furthermore, the rotational Raman spectra of CO₂ are related to vibrational temperatures through the vibrationally averaged nuclear spin degeneracy, which is expressed in the intensity ratio between even and odd numbered Raman peaks. The elevation of the odd averaged degeneracy above thermal conditions agrees well with the elevation of vibrational temperatures of CO₂, acquired in the FTIR study.

Keywords: carbon dioxide plasma, glow discharge, rotational Raman spectroscopy, molecular composition, polarizability anisotropy, nuclear spin degeneracy

1. Introduction

The reduction of CO₂ to CO and O is an important step in the field of solar fuels. An efficient dissociation is crucial when storing renewable energy in the chemical bonds of value-added hydrocarbons [1, 2]. Extensive research is conducted to examine the exploitation of non-thermal conditions in a plasma, both experimentally [3–7] and numerically [7–11], and is often concerned with the selective excitation of the asymmetric stretch vibration of CO₂ [12–15].

Recently, we published work on time-resolved Fourier transform infrared spectroscopy (FTIR) in a pulsed CO₂ glow discharge [16], focussing on the vibrational excitation of CO₂ and CO. Dissociation efficiencies in glow discharges are expected to be low and difficult to determine with meaningful precision, though the discharges are well-defined and information on the time-dependent vibrational excitation serves well to verify (reaction rates in) numerical models. While others already reported vibrational excitation in similar discharges, both continuous [17–20] and pulsed [21], we were able to demonstrate the temporal development of rotational and vibrational temperatures of CO₂ and CO. These results have already been employed by Silva *et al* [22] for comparison and validation of a kinetic model of a CO₂ discharge.

Infrared absorption takes place over a line-of-sight and therefore provides spatially averaged information. Raman spectroscopy, on the other hand, is a technique which is not only resolved in time, but also in space. This complementary diagnostic provides insight in the spatial uniformity and local temporal development of the

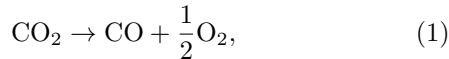
discharge.

Vibrational Raman spectroscopy is commonly used in non-thermal plasmas consisting of diatomic molecules, such as N₂, O₂, and CO, to determine rotational and vibrational temperatures, as well as number densities [23–25]. However, in the discharge under study the utilization of this technique is complicated by the vibrational modes of the triatomic CO₂: the symmetric stretch mode, two degenerate bending modes, and the asymmetric stretch mode, respectively represented by quantum numbers ν_1 , ν_2 , and ν_3 . The contribution of ν_2 to the angular momentum is designated as l_2 . The asymmetric stretch vibration is not Raman active, while a Fermi coupling between states $(\nu_1, \nu_2^{l_2}, \nu_3)$ and $((\nu_1 - 1), (\nu_2 + 2)^{l_2}, \nu_3)$ [26–28] significantly complicates the interpretation of the ν_1 and ν_2 vibrational Raman spectra.

On the other hand, *rotational* Raman spectroscopy has previously been demonstrated to be useful for measuring rotational temperatures in atmospheric-pressure dielectric-barrier discharges in CO₂ [29, 30]. An additional advantage of the technique is the ability of detecting multiple Raman active molecules in the spectral range of a single measurement, shown in e.g. atmospheric-pressure plasma jets [31, 32]. This facilitates the calibration of scattering intensity.

We employ rotational Raman spectroscopy to spatiotemporally resolve the rotational temperature and number densities of CO₂, CO, and O₂ in the same reactor and under the same discharge conditions as used in the FTIR study. The number densities are related to

the conversion of CO₂ to CO



via the conversion factor α :

$$\alpha = \frac{[\text{CO}]}{[\text{CO}] + [\text{CO}_2]}. \quad (2)$$

Here, [CO] and [CO₂] are the number densities of CO and CO₂, respectively.

Acquired insights in the uniformity are subsequently used to scrutinize the assumptions made for the analysis in the FTIR study [16]: uniform temperatures and gas composition over the line-of-sight of absorption, i.e. the length of the reactor.

Additionally, rotational Raman spectroscopy is used to examine vibrational temperatures of CO₂. In the discharge under study the vibrational modes are Treanor distributed and therefore follow vibrational temperatures T_1 , T_2 , and T_3 , respectively [18, 33]. The previously discussed Fermi coupling causes the vibrational temperatures of ν_1 and ν_2 to be equal, $T_1 = T_2 = T_{1,2}$ [26]. Excitations of vibrational modes affect the symmetry of the molecule, and therefore its nuclear degeneracy. In practice, this is expressed in a varying ratio between the intensity of even and odd numbered CO₂ peaks [34–36]. Hence, this ratio is used to scrutinize the vibrational temperatures measured in the FTIR study.

2. Experimental methods

2.1. Reactor and rotational Raman setup

The plasma reactor under study is schematically shown in Fig. 1(a) and is made of Pyrex. It is cylindrically shaped with a 2 cm inner diameter and a length of 23 cm. The electrodes are positioned 17 cm apart, in a short radial extension, opposite the gas in- and outlet. The reactor is connected in series with a 50 k Ω resistor to a power supply, while two high-voltage probes (LeCroy, *PPE 20kV*) and an oscilloscope (LeCroy, *LT584M*) are used to monitor the voltage over the reactor and the resistor. The discharge current is easily monitored by dividing the 50 k Ω resistance by the measured voltage over de resistor. The reactor is operated under flowing conditions, using a pure CO₂ (Linde, *4.5 Instrument*) inflow, controlled at 7.4 sccm with a mass flow controller (Bronkhorst, *F-201CV*). The pressure is maintained constant, using a scroll pump (Pfeiffer, *ACP 15*), and a pressure gauge (Pfeiffer, *CMR 263*) with feedback to an automated valve (Pfeiffer, *EVR 116*).

For comparison purpose, the same discharge conditions apply as in the FTIR study: the pressure is kept at 6.7 mbar with a discharge current of 50 mA. The reduced electric field in these conditions is determined to be 60 Td [16]. The plasma is pulsed with an on and off time of respectively 5 ms and 10 ms. The residence time of the gas is in the order of seconds, each molecule experiencing 150 discharges, on average, before leaving the reactor.

The optical setup in Fig. 1 is used to perform *in situ* rotational Raman spectroscopy in the reactor. The

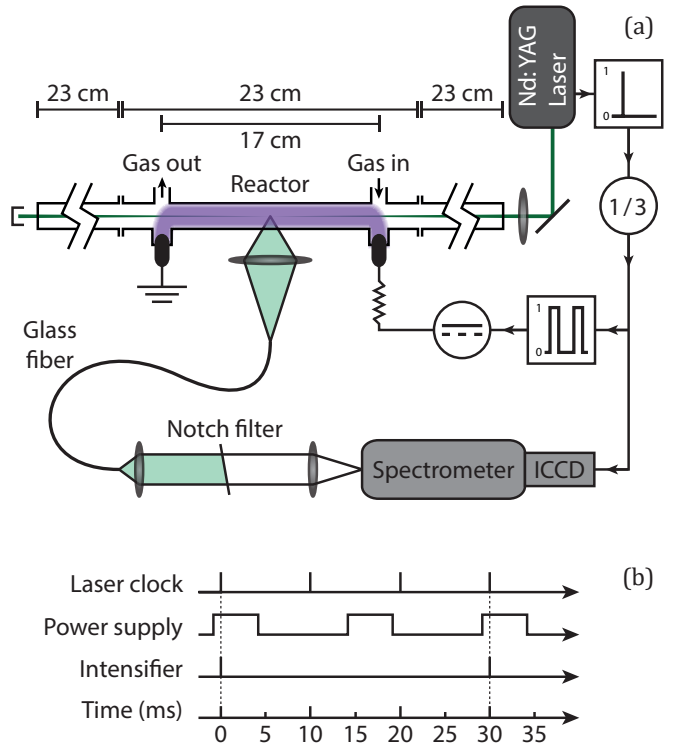


Fig. 1: (a) A schematic of the Raman setup, where the laser is focused inside the plasma reactor. The longitudinal position of measurement can be chosen by translating the reactor with respect to the focal point. The collected scattered light passes through an ultra-narrow-band notch filter to remove Rayleigh scattered and stray light. The remaining light is spectrally resolved in a spectrometer and detected with an ICCD. The clock of the laser is used to trigger both the plasma power supply and the intensifier, schematically shown in (b).

Nd:YAG laser (Spectra Physics, *Quanta-Ray, Lab-190-100*) is frequency doubled to 532 nm and operates at 100 Hz with around 140 mJ per pulse. First, the beam is expanded (not shown) using a combination of a $f = -200$ mm and a $f = 300$ mm lens, after which the beam is focused inside the plasma reactor using a $f = 1000$ mm lens, resulting in a beam waist of 70 μm . Due to heating of the laser, the lateral position of the focal point can drift over time, which is monitored by a camera (Allied Vision, *Guppy PRO F-031C*) and actively corrected with a feedback loop to a kinematic mirror mount (Polaris, *K1PZ2*) (not shown).

From the focal point, scattered light is collected with a $f = 37.5$ mm lens and focused into a glass fiber with a diameter of 200 μm . The spatial resolution of detection, i.e. the length that is imaged onto the fiber opening, is 110 μm . The exit of the fiber is used as a point source to collimate the collected light with a $f = 25$ mm lens, after which it passes through a volume Bragg grating (OptiGrate, *BragGrate, BNF-532-OD4-12.5M*). This grating acts as an ultra-narrow-band notch filter to remove Rayleigh scattered and stray light, with a full-width at half-maximum (FWHM) of 0.20 nm $\equiv 7$ cm⁻¹ and maximum attenuation of up to 0.9999 (OD 4), see [30] for more details.

A lens with a focal distance of 37.5 mm focusses the light onto the 50 μm entrance slit of the spectrometer

(Jobin-Yvon, *HR 640*, equipped with a Horiba, *530 15 Holographic Grating*, 2400 l/mm, blazed at 400 nm). The spectrally resolved light is detected with an intensified camera (ICCD), consisting of a GaAs intensifier (KATOD, *EPM102G-04-22 F*) and a Peltier cooled CCD camera (Allied Vision, *Bigeye G-132B Cool*). The frequency range of this spectrometer-ICCD combination is 183 cm^{-1} with a resolution of 0.143 cm^{-1} . The spectral broadening is determined to be Voigt shaped with a FWHM of 1.55 cm^{-1} , with an equal Gaussian and Lorentzian contribution. The wavelength sensitivity of the full detection branch is determined using the black-body radiation of a W-ribbon lamp and used for calibrating the measured spectra.

2.2. Controlling phase and position of detection

The clock of the laser is used to trigger both the power supply of the plasma reactor and the gating of the intensifier, schematically shown in Fig. 1(b). One in every three laser pulses is used to trigger two consecutive plasma pulses. In this way, the 10 ms laser period is matched with the 15 ms plasma period of 5 ms on time and 10 ms off time. The phase difference between the laser pulse and the plasma cycle is controlled by setting a delay between the laser clock and the start of the two plasma pulses.

The gate of the intensifier is triggered by one in every three laser shots, to only collect scattered light from the desired phase in the plasma cycle. The intensifier is gated for 70 ns, which is long enough to entirely cover the 10 ns laser pulse including possible jitter, but short enough to prevent significant amounts of plasma emission being recorded by the camera.

The position of detection along the longitudinal axis of the reactor is regulated by translating the reactor with respect to the focal point of the laser. With respect to previous work, the reactor has been extended by 23 cm on both sides, to avoid breaking the 532 nm AR coated windows due to too high laser energy density. For the analysis in this work, measurement positions are relative to the gas inlet of the reactor at 0.0 cm, hence the position of the gas outlet is at 17.0 cm.

2.3. Time and spatial series

A distinction is made between time and spatial series. The main purpose of the time series is to cross-check the temporal development of temperatures and molecular concentrations with the results from the FTIR study. The position of detection is fixed at 8.5 cm, at the center of the reactor, while the phase of the laser pulse is varied with respect to the plasma cycle. Time points in the plasma cycle are chosen as shown in Fig. 2, showing the temperature development obtained from the FTIR study. The selected points of 0.0, 0.7, 1.4, 2.0, 3.0, 4.9, 5.2, 6.0, 7.5, 10.0, and 12.5 ms are indicated by dotted vertical lines. Each measurement within this series has an accumulation time of 15 minutes, resulting in averaging 30,000 laser shots.

The aim of the spatial series is to examine the homogeneity of the plasma along the longitudinal axis of the reactor. The phase of the laser pulse with respect to the

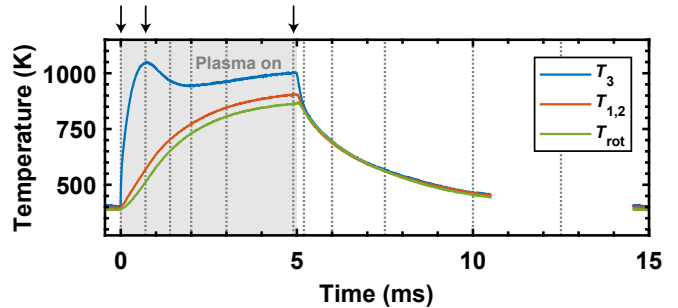


Fig. 2: Vibrational and rotational temperatures from the FTIR study [16], at a pressure of 6.7 mbar and a 50 mA plasma current, equal to the discharge conditions of the current work. Time points used for the rotational Raman time series are indicated by dotted vertical lines. Arrows point at the time points that are also used for the spatial series: 0.0 ms, 0.7 ms, and 4.9 ms.

Table 1: List of fitting parameters, including symbol, description, and guess value for the fit.

Symbol	Description	Guess
T_{rot}	Rotational temperature	600 K
N_{CO_2}	Number density of CO_2	10^{23} m^{-3}
N_{CO}	Number density of CO	10^{23} m^{-3}
N_{O_2}	Number density of O_2	10^{23} m^{-3}
$\langle g_{J,o} \rangle$	Odd avg. nuclear degeneracy of CO_2	0

plasma cycle is kept constant, while translating the reactor between measurements. The selected positions are 1.2, 3.5, 6.0, 8.5, 11.0, and 13.5 cm, where 0.0 cm and 17.0 cm are the gas in- and outlet of the reactor, respectively. Three such series are performed at time points of 0.0 ms right before the discharge, 0.7 ms where the difference between T_3 and T_{rot} is largest, and 4.9 ms at the end of the plasma pulse when a dynamic equilibrium is settling. These points are indicated by arrows in Fig. 2. A 45 minute accumulation time results in averaging 90,000 laser pulses per measurement.

2.4. Experimental procedure

The measurement procedure for a series is as follows. At the start of the series the wavelength axis is calibrated by taking a Raman spectrum of pure N_2 gas. The spectrum is also used to calibrate the Raman intensity, which is necessary for the determination of molecular number densities. Different from CO_2 , N_2 peaks are fully resolved, while at room temperatures the peaks are sufficiently strong over the full spectral range of measurement.

Hereafter the plasma cycle is started and after letting the reactor stabilize, the time or spatial measurement series is taken. The laser power is continuously monitored to adjust the intensity of the Raman spectra. Background measurements are taken while covering the fiber opening in the detection branch, blocking any scattered laser light. ICCD settings are the same as during the normal measurements.

Table 2: List of values for B (cm^{-1}), D (10^{-6} cm^{-1}), H (10^{-12} cm^{-1}), $g_{J,e}$, $g_{J,o}$, and γ at 532 nm (10^{-41} Fm^2) for CO_2 , CO , O_2 , and N_2 .

	CO_2	CO	O_2	N_2
B	0.39022 [39]	1.9225 [40]	1.4377 [41]	1.9896 [42]
D	0.1333 [39]	6.121 [40]	4.854 [41]	5.76 [42]
H	0.009 [39]	5.7 [40]	–	–
$g_{J,e}$	1 [38]	1 [38]	0 [38]	6 [38]
$g_{J,o}$	0 [38]	1 [38]	1 [38]	3 [38]
γ	23.74	6.09	12.67	7.91 [43, 44]

3. Rotational Raman scattering

The algorithm that is used to analyse the measured spectra, is designed to calculate spectrally broadened rotational Raman spectra for mixtures of different molecular species. Table 1 shows the fitting parameters that are included in a typical fit on the data. These parameters and the Raman theory on which the algorithm is based are discussed below. Special attention is given on how vibrational modes of CO_2 can influence the rotational Raman spectra through nuclear degeneracies. This is not only important for non-thermal conditions, but is shown to be relevant for thermal situations at lower temperatures as well.

3.1. Scattering in the vibrational ground state

In the event of pure rotational Raman scattering, absorption of a photon induces a rotational transition of a molecule, while a photon with a different energy gets emitted. The Raman shift, or energy difference $\Delta\tilde{\nu}$ between incident and scattered photon is of equal magnitude as the difference between initial rotational state J and final state J' , but of opposite sign [37]:

$$\Delta\tilde{\nu} = \tilde{\nu}_L - \tilde{\nu}_{J \rightarrow J'} = -(E_{\text{rot},J} - E_{\text{rot},J'}). \quad (3)$$

Here $\tilde{\nu}_L = 1/\lambda_L$ is the energy of the incident photon with wavelength λ_L , and $\tilde{\nu}_{J \rightarrow J'}$ the energy of the scattered photon. For linear molecules, only transitions of $J' = J \pm 2$ are allowed, where Stokes scattering refers to scattering with a positive $\Delta\tilde{\nu}$, and anti-Stokes scattering to a negative $\Delta\tilde{\nu}$ [37, 38].

The energy of rotational state J can be calculated using the molecular species dependent rotational constant B , centrifugal distortion constant D , and third order correction factor H and is given by [39]

$$E_{\text{rot},J} = BJ(J+1) - DJ^2(J+1)^2 + HJ^3(J+1)^3. \quad (4)$$

Values for these constants are listed in Table 2 for the molecules relevant in this study¹. H is significant for very high rotational levels J , and in the spectral range under study becomes only relevant for the position of CO_2 peaks.

¹For O_2 , the rotational levels are subdivided into triplets due to its non-zero total spin ($S = 1$). As a result, every rotational Raman peak is accompanied by two smaller satellites of which the intensities strongly decrease with increasing peak number. Furthermore, Rayleigh satellites should be present at $\pm 2 \text{ cm}^{-1}$, but these are too strongly attenuated by the notch filter to be visible in the measurements under study. Transition energies and cross-sections are included in the calculations as described in [45–47].

Furthermore, B , D , and H are different for different vibrational states, shifting the peak positions to lower or higher frequencies [39]. However, these shifts are small compared to the spectral broadening in this work, while accurate vibrational densities are not known from rotational Raman spectroscopy. Therefore, the rotational constants of vibrationally excited molecules are approximated by the vibrational ground state values of B , D , and H .

The scattering intensity $P_{J \rightarrow J'}$ of rotational Raman transition $J \rightarrow J'$ is given by [37, 43]

$$P_{J \rightarrow J'} = C n_J \frac{\partial \sigma_{J \rightarrow J'}}{\partial \Omega} \quad (5)$$

Here, n_J is the number density of molecules in rotational state J , and $\frac{\partial \sigma_{J \rightarrow J'}}{\partial \Omega}$ the transition dependent differential scattering cross-section. The constant C is the product of molecular and rotational state independent constants, such as the laser intensity, detection path length, and solid angle of detection.

For the density n_J the rotational states are assumed to be Boltzmann distributed:

$$n_J = \frac{N g_{\text{rot},J}}{Q_{\text{rot}}} \exp\left(-\frac{hcE_{\text{rot},J}}{k_B T_{\text{rot}}}\right), \quad (6)$$

where N is the number density of the molecular species, h is Planck's constant, c is the speed of light, k_B is the Boltzmann constant, and T_{rot} is the rotational temperature. T_{rot} is assumed to be the same for all molecular species and equal to the translational temperature [18]. $g_{\text{rot},J}$ is the total degeneracy of rotational state J and is the product of the rotational degeneracy $2J + 1$ and the nuclear degeneracy which is listed in Table 2 as $g_{J,e}$ and $g_{J,o}$, for even and odd values for J , respectively [37]. The rotational partition sum Q_{rot} is calculated using the method of McDowell *et al* [48] and normalizes n_J , such that its sum over all J is equal to N .

The differential scattering cross-section is dependent on the polarization of the laser beam and the angle of detection, and varies for different polarizations of the scattered light. The Raman spectrometer from Fig. 1 detects scattered light of all polarizations, collected perpendicular to both the beam direction and its linear polarization. The differential cross-section is then given by [37]

$$\frac{\partial \sigma_{J \rightarrow J'}}{\partial \Omega} = \frac{7}{45} \frac{\pi^2}{\varepsilon_0^2} \gamma^2 b_{J \rightarrow J'} \tilde{\nu}_{J \rightarrow J'}^4. \quad (7)$$

Here, ε_0 is the vacuum permittivity, and $b_{J \rightarrow J'}$ is the Placzek-Teller coefficient as can be found in [37, 43, 49]. The polarizability anisotropy γ is dependent on the molecular species and the incident wavelength and is listed in Table 2. Values are determined from calibration Raman measurements on pure CO_2 , CO , O_2 , and N_2 gas, shown in Fig. 3. The intensities correspond to an equal number density for every molecular species, while the spectra are normalized to the maximum of the CO_2 spectrum. γ can now easily be determined from a fit on the data (solid black lines), since the intensity of a spectrum is linearly proportional to γ^2 . Values for CO_2 , O_2 , and CO are calculated with respect to the value for N_2 , which is taken as the mean from Penney *et al* [43] and

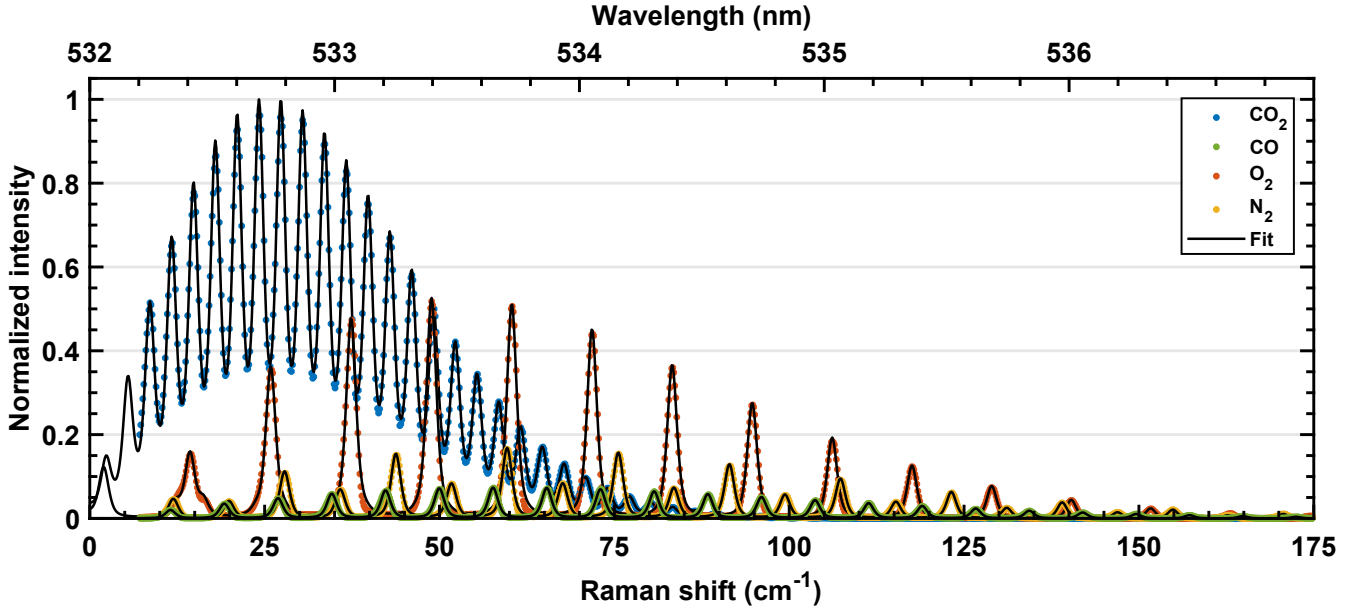


Fig. 3: Rotational Raman spectra (Stokes only) of pure CO₂, CO, O₂, and N₂ gas at room temperature. The spectra are normalized to the maximum of the CO₂ spectrum.

Bogaard *et al* [44]. Penny *et al* also provide γ for CO₂ and O₂, while Bogaard *et al* report anisotropies of CO₂ and CO. The values determined from Fig. 3 stay within their reported expected errors.

Spectral broadening is applied to the calculated peak positions and intensities in the form of a Voigt profile with the previously introduced FWHM of 1.55 cm⁻¹. The total spectrum is then obtained by adding up the calculated spectra of all individual molecular species.

3.2. Nuclear degeneracies of vibrationally excited CO₂

The J dependent nuclear degeneracies listed in Table 2 are only valid when the molecule is in its vibrational ground state or in a vibrational state of equal symmetry, as described in [34–36]. The single vibrational mode of diatomic molecules, such as CO, O₂, and N₂, meets this requirement and therefore degeneracies stay the same for any vibrational excitation. Similarly, CO₂ maintains its ground state symmetry when it is purely excited in the symmetric stretch mode (ν_1). The symmetry changes, however, when the bending mode (ν_2) or asymmetric stretch mode (ν_3) is excited.

In the case of ν_2 excitation, the nuclear degeneracies become [$g_{J,e} = 1, g_{J,o} = 1$], for any combination of ν_1 and ν_3 . When ν_3 is excited, while ν_2 is not, the degeneracies alternate between [$g_{J,e} = 1, g_{J,o} = 0$] and [$g_{J,e} = 0, g_{J,o} = 1$] for even and odd ν_3 levels, respectively. This again holds for any excitation of ν_1 . See [34–36] for more details.

As previously mentioned, the positions of pure rotational peaks just weakly depend on vibrations and therefore overlap for molecules in different vibrational states. Information on vibrational state densities of CO₂ can then be acquired by substituting $g_{J,e}$ and $g_{J,o}$ by the vibrationally averaged nuclear degeneracies $\langle g_{J,e} \rangle$ and

$\langle g_{J,o} \rangle$ [36]:

$$\langle g_{J,e/o} \rangle = \frac{1}{2} \pm \frac{1}{2} \frac{1 - z_2}{1 + z_2} \frac{1 - z_3}{1 + z_3}, \quad (8)$$

where the plus sign belongs to the even degeneracy. These averaged degeneracies are related to the vibrational temperatures through z_i , which is defined using the harmonic approximation for vibrational energy levels as [36]

$$z_i = \exp\left(-\frac{hcG_{1,i}}{k_B T_i}\right). \quad (9)$$

Here, $G_{1,i}$ is the energy spacing between the ground and the first vibrational level of vibrational mode ν_i . The energy spacings of ν_2 and ν_3 of CO₂ are, respectively, 667.47 cm⁻¹ and 2349.16 cm⁻¹ [27]. T_i is the vibrational temperature of the mode, where T_2 is substituted by the combined vibrational temperature of ν_1 and ν_2 , $T_{1,2}$.

From Eq. (8) it is clear that $\langle g_{J,e} \rangle + \langle g_{J,o} \rangle = 1$ for any combination of vibrational temperatures. In the lower temperature limit when every CO₂ molecule is in the vibrational ground state ($z_i = 0$) the averaged degeneracies reduce back to [$\langle g_{J,e} \rangle = 1, \langle g_{J,o} \rangle = 0$]. For very high $T_{1,2}$ ($z_2 = 1$), the averaged degeneracies become [$\langle g_{J,e} \rangle = \frac{1}{2}, \langle g_{J,o} \rangle = \frac{1}{2}$]. This corresponds to the nuclear degeneracies of CO₂ in the bending mode, divided by the mode's vibrational degeneracy of 2. The same averaged degeneracies are obtained at very high T_3 , when $z_3 = 1$ and there is an equal density of even and odd ν_3 levels.

Furthermore, under thermal conditions of 400 K, right before the start of a plasma pulse (see Fig. 2), 18% of the CO₂ molecules is vibrationally excited. The corresponding averaged degeneracies are calculated to be [$\langle g_{J,e} \rangle = 0.916, \langle g_{J,o} \rangle = 0.084$]. This non-negligible deviation from ground state degeneracies demonstrates that even in low-temperature thermal conditions it is important to take into account the influence of vibrational state densities on the nuclear degeneracies.

4. Results

4.1. Rotational Raman spectra

Three examples of rotational Raman spectra, as measured during the time series, are shown in Fig. 4. The three spectra are taken in the center of the reactor, at (a) 0.0 ms, (b) 0.7 ms, and (c) 4.9 ms. The data is shown as yellow circles, while the data that is excluded from fitting due to deformation by the notch-filter profile is gray. The total fit is represented by a solid black line, and lines of different colors illustrate the contribution of CO₂, CO, and O₂ lines to this fit. Here, CO₂ is subdivided in lines coming from transitions of even rotational states (solid line) and odd states (dotted line).

The total fit accurately describes the data in all panels, clearly showing the relation between increasing rotational temperature and increased scattering intensity at larger Raman shifts. Peaks of CO and O₂ are most explicit at larger shifts, where the intensity of CO₂ peaks drops significantly. At higher temperatures CO and O₂ still exceed CO₂, visible in panel (c). In contrast to CO, O₂ peaks also significantly contribute to the total fit at smaller Raman shifts (see peaks at 61 cm⁻¹, 72 cm⁻¹, and 84 cm⁻¹). Fitted O₂ densities are therefore generally more accurate than CO densities.

Furthermore, the panels show three distinct situations regarding the contribution of even and odd CO₂ peaks at three time points in the on-off cycle of the pulsed plasma, indicated by an arrow in Fig. 2. In panel (a), at the start of the plasma pulse, the gas is in thermal equilibrium and relatively cool at 394 K. The odd vibrationally averaged nuclear degeneracy of CO₂ is still low, but the contribution of odd peaks is visible in the peak minima of the total fit. In panel (c), at the end of the plasma pulse, the vibrational temperatures of CO₂ are expected to exceed the rotational temperature of 809 K only marginally (see Fig. 2). Also visible in panel (c), the broadening of peaks below 100 cm⁻¹ seems increased with respect to the broadening in panel (a). The even CO₂ peaks strongly underfit the data at the peak minima, which is compensated by an increase of $\langle g_{J,o} \rangle$ and therefore the fraction of odd peaks.

In panel (b) at 0.7 ms in the plasma, T_{rot} is still low relative to (c), but the fraction of odd CO₂ peaks is comparable. The fitted odd averaged degeneracy exceeds the degeneracy that is expected if the gas would be thermal at T_{rot} , which indicates an elevation of vibrational temperatures. This is subject to further discussion in section 4.4.

4.2. Temperature profile

The temperatures determined from the spatial and time series are shown in Fig. 5(a) and (b), respectively, including a 95% fitting uncertainty. Data points from the spatial series which were acquired in the center of the reactor are also shown in the time series of panel (b), indicated by diamonds. Similarly, temperatures at 0.0 ms, 0.7 ms, and 4.9 ms in the time series are plotted as diamonds in panel (a). The rotational temperatures of both series agree well on corresponding time and position, showing good reproducibility over different

experimental sessions. The fitted rotational temperature mainly relies on the overall shape of the spectrum and less on the quality of individual peaks, i.e. the signal-to-noise ratio, and is insensitive to variations in laser intensity.

For the analysis of the FTIR study it is assumed that the rotational temperature is constant over the line-of-sight of IR absorption. This assumption is confirmed by the spatial series, showing a uniform temperature along the length of the reactor. There is only a small decrease in temperature at 1.2 cm, close to the entrance. Here, the gas enters the reactor with a temperature around 300 K and reaches its steady state value within a short distance relative to the total length of the reactor.

The time series is compared to the rotational temperature profile from the FTIR study, which is represented by a solid line in panel (b). Qualitatively and quantitatively there is good agreement between the temperature development in both studies: an initial temperature of 400 K quickly increases at ignition, but levels off around 800 K at the end of the plasma pulse, where the results from the FTIR study exceed the temperatures from Raman up to 60 K. T_{rot} exponentially decreases in the off time towards the initial temperature.

4.3. Molecular number densities

The fitted number densities of CO₂, CO, and O₂ are shown for the spatial series in Fig. 6(a) and for the time series in Fig. 7(a), including a 95% fitting uncertainty. Diamonds indicate number densities that are measured in the other series. The solid lines in Fig. 7 represent results from the FTIR study, where the O₂ density is assumed to be half the CO density, following Eq. (1). O₂ could not be directly determined with IR absorption, since its vibrational mode is IR inactive.

The total molecular number density is assumed to be the sum of the densities of CO₂, CO, and O₂. This assumption is supported by the fact that apart from CO₂ and CO no other IR active molecules are detected in the FTIR study, and that the rotational Raman spectra in Fig. 4 show no indication of other rotationally active species. However, both techniques cannot detect atomic oxygen, while some amounts are likely formed [50], which is subject of future study. Though, no large amounts of atomic oxygen are expected in the conditions under study, since the average ratio of CO over O₂ as measured with Raman spectroscopy is close to 2, for every measurement series: 2.2 ± 0.3 for the time series and 1.8 ± 0.3 , 1.8 ± 0.3 , and 1.8 ± 0.4 for the spatial series at 0.0 ms, 0.7 ms, and 4.9 ms, respectively.

Number densities vary strongly between different time points during the plasma cycle, which is best observed in Fig. 7(a). All number densities drop when the discharge starts, leveling off at the end of the pulse, after which the number densities slowly relax back to the initial value. This profile is qualitatively the inverse of the temperature profile, which is expected from the ideal gas law: as the molecules heat up, the pressure will increase and the gas starts expanding, decreasing the number densities.

The reduction in total number density from start to end of the discharge is 50% and 38% for Raman and

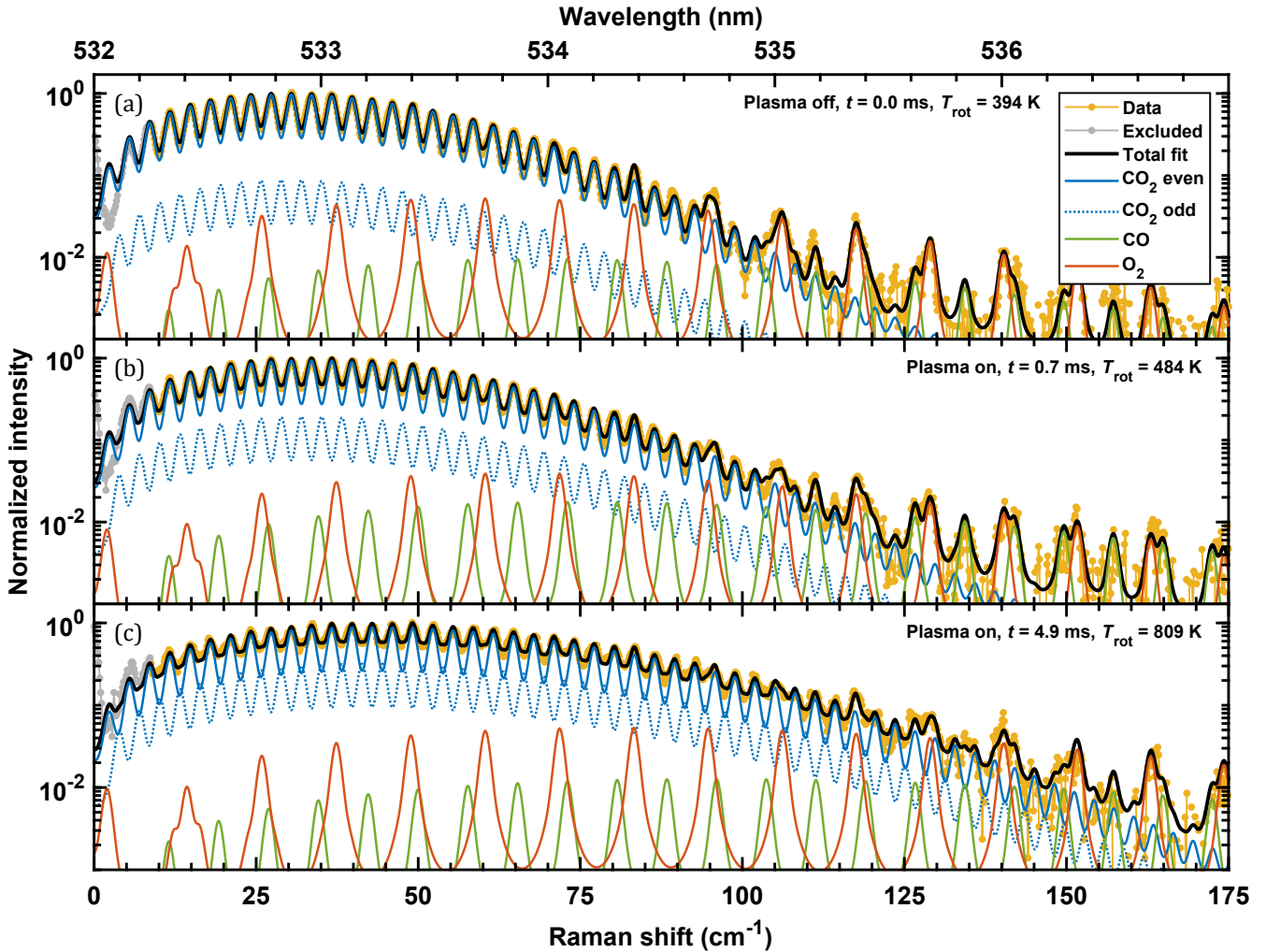


Fig. 4: Three examples of rotational Raman spectra (Stokes only) measured at 8.5 cm, in the center of the reactor. The measurements are taken at (a) 0.0 ms, (b) 0.7 ms, and (c) 4.9 ms in a 5-10 ms on-off sequence. The accumulation time is 45 minutes, averaging 90,000 laser shots. The fit on the data is indicated by a solid black line, while the contributions of even and odd CO₂ peaks, CO, and O₂ peaks are shown separately.

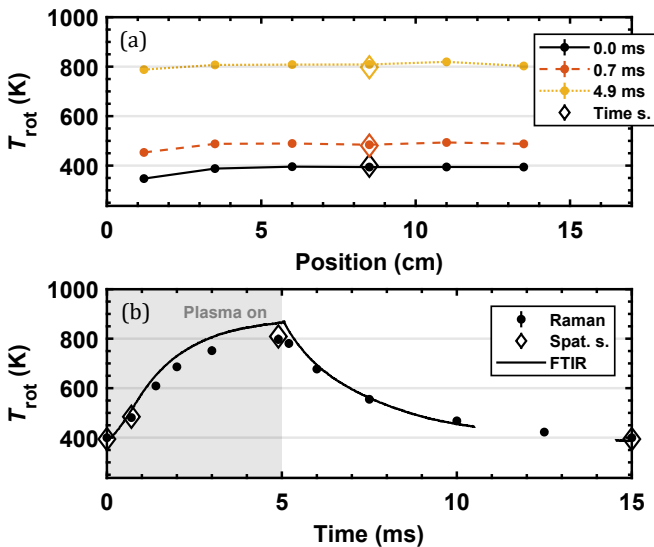


Fig. 5: The rotational temperature versus (a) position and (b) time. Points at equal position and timing, but measured during the other series are indicated with diamonds. The rotational temperature from the FTIR study is added in panel (b) as a solid line [16].

FTIR, respectively. This is well explained by the reactor extensions: when the plasma heats up, it is easier for the gas to expand into the extension volume than through the narrow in- and outlet.

To discuss the relative composition of the gas, panel (b) of Figs. 6 and 7 show the composition proportional to the total number density. The CO₂ conversion factor α , see Eq. (2), is plotted in panel (c). The accuracy of α is strongly dependent on the accuracy of the fitted number density of CO. α is therefore represented as the weighted mean from two calculations for which the inverse variance is calculated from the variance of the fitted parameters and serves as weight: (1) using the fitted densities of CO₂ and CO, and (2) substituting the density of CO by twice the more accurately fitted density of O₂.

During the FTIR analysis the spatial profile of the gas composition was treated as homogeneous. Scrutinizing this assumption, the composition is indeed uniform over the length of the reactor (Fig. 6(b) and (c)), despite using pure CO₂ as initial gas. It is known from the FTIR study that in pure CO₂ the conversion per discharge cycle is below the detection limit of <0.005 [16]. Raman measurements are performed at its closest 1.2 cm from the gas inlet, which is a distance in which molecules ex-

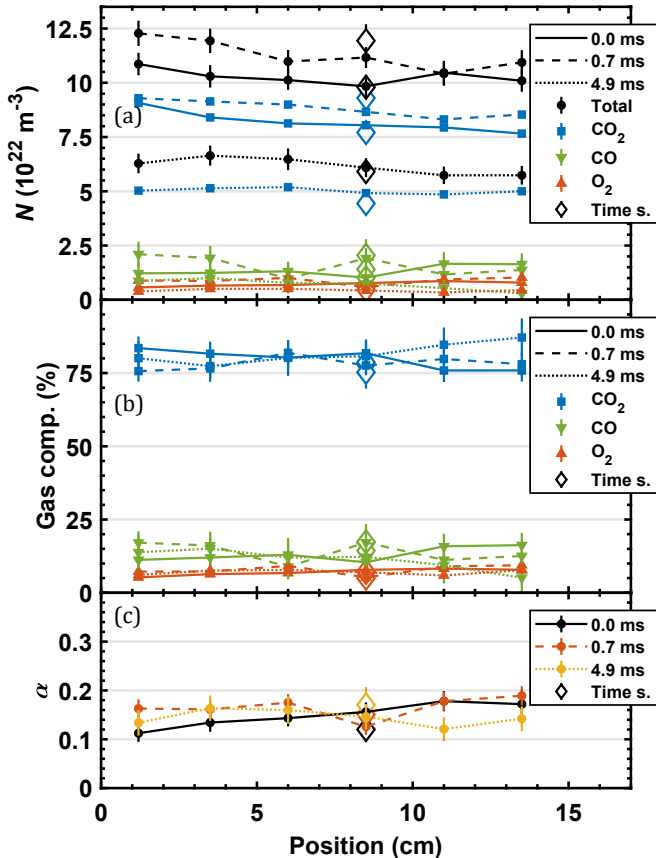


Fig. 6: Fitting results from the rotational Raman spatial series. (a) Absolute molecular number densities of CO_2 , CO, O_2 , and all three combined (total). (b) The gas composition, assuming other species than CO_2 , CO, and O_2 are not present in significant amounts. (c) The conversion factor α . In all panels, diamonds indicate points at equal position and timing measured during the spatial series.

perience on average 10 discharge cycles. The expected conversion at 1.2 cm of $\alpha < 0.05$ is clearly below the measured value of 0.11–0.17, visible in the graph.

This can be explained by two phenomena in gas dynamics that stimulate gas mixing over the full length of the reactor. First, the contribution of diffusion to this mixing can be assessed by calculating the Péclet number for mass transfer [51]:

$$Pe = \frac{Lu}{D}, \quad (10)$$

where L is the length of the discharge volume, u is the average flow velocity (L divided by the residence time), and D is the pressure and temperature dependent diffusion coefficient [52]. The Péclet number represents the ratio of mass transfer by motion to mass transfer by diffusion and in the conditions under study is $Pe \approx 5$. Since Pe is close to one, both forms of mass transfer are of similar importance, hence one would expect some gradient towards the gas outlet, but diffusion plays a significant role in gas mixing.

Secondly, uniformity is stimulated by convection as a result from the gas expansion during the discharge. The repetitive expansion and contraction (Fig. 7(a)), respectively caused by the heating and cooling of the discharge region, stimulates molecules from various locations to

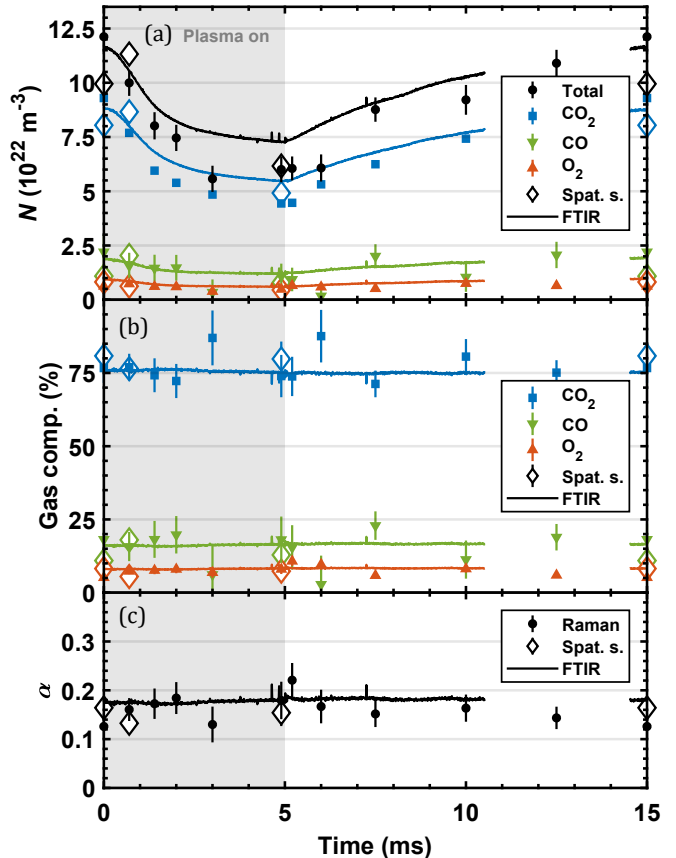


Fig. 7: Fitting results from the rotational Raman time series. (a) Absolute molecular number densities of CO_2 , CO, O_2 , and all three combined (total). (b) The gas composition, assuming other species than CO_2 , CO, and O_2 are not present in significant amounts. (c) The conversion factor α . In all panels, diamonds indicate points at equal position and timing measured during the spatial series, while the solid lines originate from the FTIR study [16].

mix, increasing the homogeneity over the length of the reactor. Although the reactor extensions facilitate an increased expansion, a comparable spatial uniformity is expected for the FTIR study. This is supported by a similar composition and, hence, conversion in the center of the reactor as can be seen in Fig. 7(b) and (c). The time averaged conversion factor of 0.15 ± 0.02 , obtained from the Raman measurements, is close to the time averaged factor of 0.18 in the FTIR study.

4.4. Vibrational temperatures

In this section the fitted vibrationally averaged nuclear degeneracy of odd rotational levels of CO_2 is discussed. To this purpose, Eq. (8) is used to make a contour plot of the odd averaged degeneracy versus $T_{1,2}$ and T_3 , shown in Fig. 8. The isothermal is indicated with a diagonal line.

The fitting results of the spatial series at 0.7 ms and 8.5 cm are added to illustrate how this representation can aid in interpreting the implications of a fitted averaged degeneracy. The fitted rotational temperature of 484 K is assumed to be the lower limit for both vibrational temperatures, hence the area where either temperature is lower is omitted, indicated by a blue shading. The fitted odd averaged degeneracy of 0.171 is then indicated in

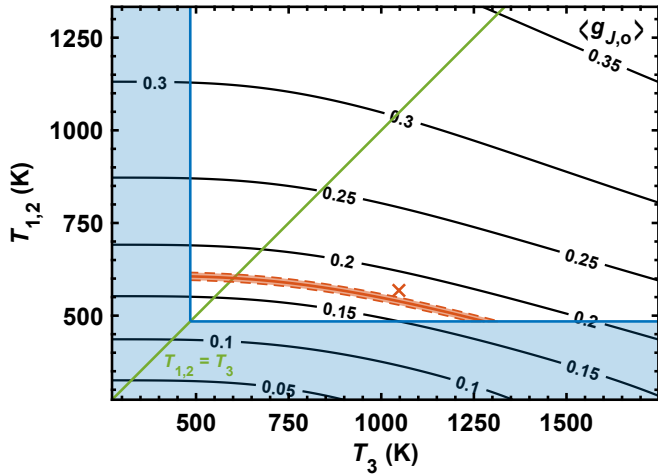


Fig. 8: A contour map of the odd vibrationally averaged nuclear degeneracy of CO₂ as function of $T_{1,2}$ and T_3 . The diagonal line marks the isothermal. Fitting results of the spatial series at 0.7 ms and 8.5 cm are indicated as follows: the blue shaded area demarcates the temperature region below the fitted rotational temperature of 488 K, while the orange curve indicates the fitted odd averaged degeneracy of 0.171 in a band with a half-width of the 95% fitting uncertainty. The fitted $T_{1,2}$ and T_3 as measured under equal discharge conditions during the FTIR study are indicated by an orange cross [16].

the remainder of the contour plot by an orange curve, including a band with a half-width equal to the 95% fitting uncertainty. Now, the expected values of $T_{1,2}$ and T_3 are such that the combination intersects with this band.

Although this combination of temperatures is not conclusive to a high degree, the map serves well for indicating upper temperature limits, being 606 ± 10 K and 1279 ± 40 K for $T_{1,2}$ and T_3 , respectively. Additionally, the odd averaged degeneracy can well be used to evaluate the vibrational temperatures acquired in the FTIR study. These values are $T_{1,2} = 568$ K and $T_3 = 1048$ K, indicated by an orange cross, close to the fitted odd averaged degeneracy. This affirms the concept of using the degeneracy as an indication for vibrational excitation and supports the vibrational temperatures as measured in the FTIR study.

To continue the comparison between the vibrational excitation in both studies, the odd vibrationally averaged nuclear degeneracy is plotted versus position in Fig. 9(a). Error bars indicate a 95% fitting uncertainty. The gray data points and lines indicate the expected odd averaged degeneracy if the plasma would be thermalized at T_{rot} , i.e. $T_{1,2} = T_3 = T_{\text{rot}}$. Elevations above this calculation are an indication for non-thermal conditions. Averaged degeneracies which are measured at similar time points or position, but during the time series are again depicted as diamonds.

As previously shown in Fig. 4, $\langle g_{J,o} \rangle$ is sensitive to the apparent broadening of CO₂ peaks and is affected by broadening increasing events, such as wavelength shifts/jitter of the spectra during camera accumulation. Therefore, the actual error is expected to be larger than the fitting error.

Panel (a) in Fig. 9 shows that the odd averaged degeneracy is almost constant over space. This indicates

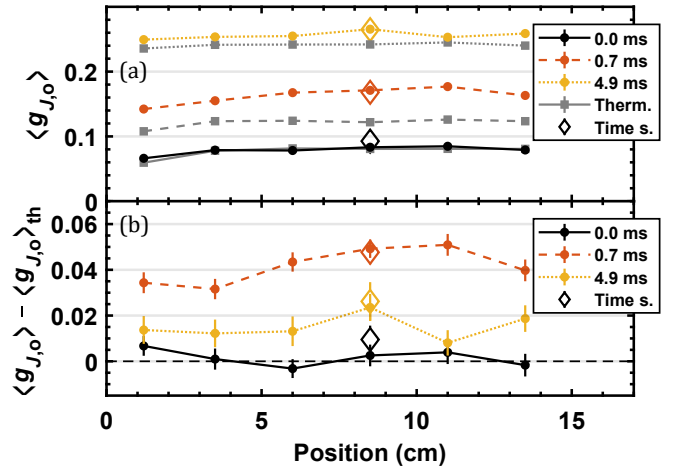


Fig. 9: Fitting results from the spatial Raman series. (a) The odd vibrationally averaged nuclear degeneracy of CO₂ (colored) including the expected odd averaged degeneracy under thermal conditions, calculated using the fitted rotational temperature (gray, corresponding line style). (b) The difference between the fitted odd averaged degeneracy and the calculated odd degeneracy assuming thermal conditions. In both panels, diamonds indicate points at equal position and timing measured during the time series.

only small variation in vibrational temperatures over the length of the reactor. In panel (b), the difference is shown between the fitted odd averaged degeneracy and the calculated degeneracy at thermalization with temperature T_{rot} , representing the absolute excitation of the odd averaged degeneracy. The degeneracy at 0.0 ms is consistently not excited above thermal level, as is expected right before the start of the plasma pulse. At other time points, excitations follow expectations as well: at 0.7 ms, when the elevation of T_3 above T_{rot} is largest, the odd averaged degeneracy exceeds thermal level to a larger extent than at 4.9 ms, where the vibrational and rotational temperatures are again closer to equilibrium (see Fig. 2).

The temporal analysis is continued with the time series in Fig. 10, where panels (a) and (b) show similar plots as in Fig. 9. Additionally, temperatures of the FTIR study are used to calculate the expected excitation of odd averaged degeneracies, shown as a black curve in panel (b).

In both panels it can be seen that during the discharge the odd averaged degeneracy is continuously above thermal level, while during the off time the degeneracy directly relaxes. The point at 7.5 ms is an exception to this and is presumably an outlier, illustrating the previously discussed error and sensitivity to irregular external factors. Panel (b) shows good agreement between the fitted excitation and the excitation calculated from the FTIR study: both quickly increase at the start of the discharge, where T_3 rapidly rises when the rotational temperature is still low. Hereafter, T_3 drops and levels off when the plasma stabilizes to a situation which is closer to equilibrium between vibrational and rotational temperatures.

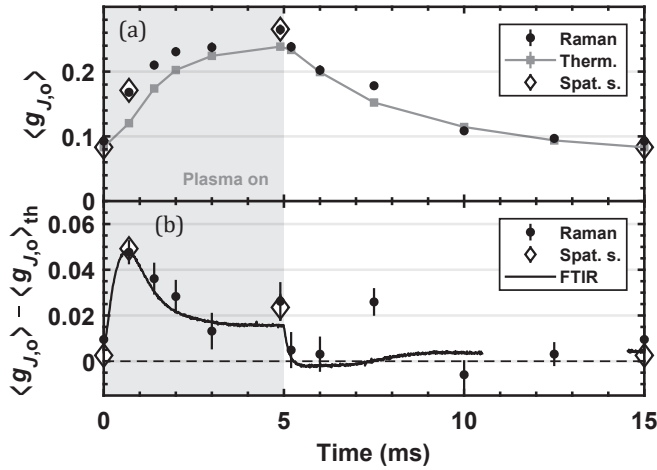


Fig. 10: Fitting results from the rotational Raman time series. (a) The odd vibrationally averaged nuclear degeneracy of CO_2 (black) including the expected odd averaged degeneracy under thermal conditions, calculated using the fitted rotational temperature (gray). (b) The difference between the fitted odd averaged degeneracy and the calculated odd degeneracy assuming thermal conditions. In both panels, diamonds indicate points at equal position and timing measured during the spatial series. The solid line in (b) is calculated from the results of the FTIR study [16]. The data point at 7.5 ms is arguably an outlier (see text).

5. Conclusions

Spatial and time resolved rotational Raman spectroscopy is performed in a pulsed CO_2 glow discharge. Spectra that are recorded at several time points during the discharge cycle show distinctive contributions of peaks of CO_2 , CO , and O_2 molecules. This holds for any rotational temperature in the conditions under study, ranging from 400 K to well above 800 K. Contributions of CO_2 peaks can be recognized as originating from even or odd rotational levels. The underlying vibrationally averaged nuclear degeneracies are directly related to the vibrational temperatures of CO_2 .

The rotational temperature during the discharge is determined to be homogeneous over the length of the reactor, which confirms the assumption that the rotational temperature is constant over the line-of-sight of absorption in the FTIR study [16]. Furthermore, the temporal development of the rotational temperature agrees qualitatively and quantitatively with the FTIR study.

The gas compositions acquired from the Raman spectra agree well with the results in the FTIR study. The composition is shown to be homogeneous over the length of the reactor, confirming a second assumption made during the IR absorption analysis. The homogeneity is attributed to gas mixing, stimulated by diffusion and the gas expansion during the discharge. The extensions in the reactor configuration under study facilitate an increased expansion, though differences in number densities with the FTIR study are much smaller than the total change in number density during the discharge.

The vibrational temperatures are demonstrated to be related to the vibrationally averaged nuclear degeneracies. The fitted odd averaged degeneracy is used to find the relation between $T_{1,2}$ and T_3 , including their upper

limits. Additionally, the odd averaged degeneracy is useful for the validation of vibrational temperatures which are determined from other diagnostics. A comparison with the FTIR study, shows good agreement between vibrational temperatures and odd averaged degeneracy, supporting the IR absorption analysis.

Acknowledgements

This work is partially funded by the Netherlands Organisation for Scientific Research (NWO), under references 713.013.003 and 10018663 (NWO Duurzaam), partially by the Portuguese Foundation for Science and Technology (FCT) under grant PD/BD/105884/2014 (PD-F APPLAuSE), and partially by LABEX Plas@par receiving financial aid managed by the French National Research Agency (ANR) under reference ANR-16-CE06-0005.

References

- [1] Centi G, Quadrelli E A and Perathoner S 2013 *Energy & Environmental Science* **6** 1711 ISSN 1754-5692 URL <http://xlink.rsc.org/?DOI=c3ee00056g>
- [2] Bogaerts A, Kozák T, van Laer K and Snoeckx R 2015 *Faraday Discuss.* **183** 217–232 ISSN 1359-6640 URL <http://xlink.rsc.org/?DOI=C5FD00053J>
- [3] Brehmer F, Welzel S, van de Sanden M C M and Engeln R 2014 *Journal of Applied Physics* **116** 123303 ISSN 0021-8979 URL <http://aip.scitation.org/doi/10.1063/1.4896132>
- [4] Yap D, Tatibouët J M and Batiot-Dupeyrat C 2015 *Journal of CO₂ Utilization* **12** 54–61 ISSN 22129820 URL <http://linkinghub.elsevier.com/retrieve/pii/S2212982015300081>
- [5] Bongers W, Bouwmeester H, Wolf B, Peeters F, Welzel S, van den Bekerom D, den Harder N, Goede A, Graswinckel M, Groen P W, Kopecki J, Leins M, van Rooij G, Schulz A, Walker M and van de Sanden R 2017 *Plasma Processes and Polymers* **14** 1600126 ISSN 16128850 URL <http://doi.wiley.com/10.1002/ppap.201600126>
- [6] Huang Q, Zhang D, Wang D, Liu K and Kleyn A W 2017 *Journal of Physics D: Applied Physics* **50** 294001 ISSN 0022-3727 URL <http://stacks.iop.org/0022-3727/50/i=29/a=294001?key=crossref.e8b01256eb576a7cb25681b5f404d74d>
- [7] Moss M S, Yanallah K, Allen R W K and Pontiga F 2017 *Plasma Sources Science and Technology* **26** 035009 ISSN 1361-6595 URL <http://stacks.iop.org/0963-0252/26/i=3/a=035009?key=crossref.6487d973b186735a688953d689510dd0>
- [8] Pietanza L, Colonna G, D’Ammando G, Laricchiuta A and Capitelli M 2016 *Chemical Physics* **468** 44–52 ISSN 03010104 URL

- <http://linkinghub.elsevier.com/retrieve/pii/S0301010415300823>
- [9] de la Fuente J F, Moreno S H, Stankiewicz A I and Stefanidis G D 2016 *React. Chem. Eng.* **1** 540–554 ISSN 2058-9883 URL <http://xlink.rsc.org/?DOI=C6RE00044D>
- [10] Grofulović M, Alves L L and Guerra V 2016 *Journal of Physics D: Applied Physics* **49** 395207 ISSN 0022-3727 URL <http://stacks.iop.org/0022-3727/49/i=39/a=395207?key=crossref.787fe3f190485085b33f7cf97078474f>
- [11] Koelman P, Heijkers S, Tadayon Mousavi S, Graef W, Mihailova D, Kozak T, Bogaerts A and van Dijk J 2017 *Plasma Processes and Polymers* **14** 1600155 ISSN 16128850 URL <http://doi.wiley.com/10.1002/ppap.201600155>
- [12] Capezzuto P, Cramarossa F, D'Agostino R and Molinari E 1976 *The Journal of Physical Chemistry* **80** 882–888 ISSN 0022-3654 URL <http://pubs.acs.org/doi/abs/10.1021/j100549a024>
- [13] Legasov V A, Zhivotov V K, Krasheninnikov E G, Krotov M F, Patrushev B I, Rusanov V D, Rykunov G V, Spektor A M, Fridman A A and Sholin G V 1978 *Soviet Physics Doklady* **238** 66–69
- [14] Fridman A 2008 *Plasma Chemistry* (New York: Cambridge University Press) ISBN 9780521847353
- [15] Snoeckx R and Bogaerts A 2017 *Chem. Soc. Rev.* **46** 5805–5863 ISSN 0306-0012 URL <http://xlink.rsc.org/?DOI=C6CS00066E>
- [16] Klarenaar B L M, Engeln R, van den Bekerom D C M, van de Sanden M C M, Morillo-Candas A S and Guaitella O 2017 *Plasma Sources Science and Technology* **26** 115008 ISSN 1361-6595 URL <http://iopscience.iop.org/article/10.1088/1361-6595/aa902e> <http://stacks.iop.org/0963-0252/26/i=11/a=115008?key=crossref.48b81f0a184d89f41bc9714ee4911ab3>
- [17] Siemsen K, Reid J and Dang C 1980 *IEEE Journal of Quantum Electronics* **16** 668–676 ISSN 0018-9197 URL <http://ieeexplore.ieee.org/document/1070536/>
- [18] Dang C, Reid J and Garside B K 1982 *Applied Physics B Photophysics and Laser Chemistry* **27** 145–151 ISSN 0721-7269 URL <http://link.springer.com/10.1007/BF00694640>
- [19] Andreev S N and Savinov S Y 1995 *Bulletin of the Lebedev Physics Institute* **6** 26–30
- [20] Andreev S N, Zakharov V V, Ochkin V N and Savinov S Y 2004 *Spectrochimica Acta Part A: Molecular and Biomolecular Spectroscopy* **60** 3361–3369 ISSN 13861425 URL <http://linkinghub.elsevier.com/retrieve/pii/S1386142504001143>
- [21] Rivallan M, Aiello S and Thibault-Starzyk F 2010 *Review of Scientific Instruments* **81** 103111 ISSN 00346748 URL <http://scitation.aip.org/content/aip/journal/rsi/81/10/10.1063/1.3492094>
- [22] Silva T, Grofulović M, Klarenaar B L M, Morillo-Candas A S, Guaitella O, Engeln R, Pintassilgo C D and Guerra V 2018 *Plasma Sources Science and Technology* **27** 015019 ISSN 1361-6595 URL <http://iopscience.iop.org/article/10.1088/1361-6595/aaa56a> <http://stacks.iop.org/0963-0252/27/i=1/a=015019?key=crossref.6e57c8ab3f1e816afdab544f654d987d>
- [23] Lo A, Cessou A, Boubert P and Vervisch P 2014 *Journal of Physics D: Applied Physics* **47** 115201 ISSN 0022-3727 URL <http://stacks.iop.org/0022-3727/47/i=11/a=115201?key=crossref.3f7a72fefec683e713346830ef7f4877>
- [24] Lee W, Adamovich I V and Lempert W R 2001 *The Journal of Chemical Physics* **114** 1178–1186 ISSN 0021-9606 URL <http://aip.scitation.org/doi/10.1063/1.1332400>
- [25] Lempert W R and Adamovich I V 2014 *Journal of Physics D: Applied Physics* **47** 433001 ISSN 0022-3727 URL <http://stacks.iop.org/0022-3727/47/i=43/a=433001?key=crossref.7510001fce8102d5f1ede7d2a62c369c>
- [26] Wittman W J 1987 *The CO₂ Laser* (Berlin, Heidelberg: Springer-Verlag) ISBN 3540176578
- [27] Suzuki I 1968 *Journal of Molecular Spectroscopy* **25** 479–500 ISSN 00222852 URL <http://www.sciencedirect.com/science/article/pii/S0022285268800189>
- [28] Amat G and Pimbert M 1965 *Journal of Molecular Spectroscopy* **16** 278–290 ISSN 0022-2852 URL <http://www.sciencedirect.com/science/article/pii/0022285265901232>
- [29] Brehmer F, Welzel S, Klarenaar B L M, van der Meiden H J, van de Sanden M C M and Engeln R 2015 *Journal of Physics D: Applied Physics* **48** 155201 ISSN 0022-3727 URL <http://stacks.iop.org/0022-3727/48/i=15/a=155201?key=crossref.a5b775f4d14dadd1fcadb1b98ac51b1>
- [30] Klarenaar B L M, Brehmer F, Welzel S, van der Meiden H J, van de Sanden M C M and Engeln R 2015 *Review of Scientific Instruments* **86** 046106 ISSN 0034-6748 URL <http://scitation.aip.org/content/aip/journal/rsi/86/4/10.1063/1.4918730>
- [31] van Gessel A F H, Carbone E A D, Bruggeman P J and van der Mullen J J A M 2012 *Plasma Sources Science and Technology* **21** 015003 ISSN 0963-0252 URL <http://stacks.iop.org/0963-0252/21/i=1/a=015003?key=crossref.e16a00ad074075da0945bb1f1b69bff7>

- [32] Hübner S, Sousa J S, van der Mullen J and Graham W G 2017 *Plasma Sources Science and Technology* **24** 054005 ISSN 0963-0252 URL <http://stacks.iop.org/0963-0252/24/i=5/a=054005?key=crossref.53e9e135192e522d7d771aaa4fb71b92>
- [33] Treanor C E 1968 *The Journal of Chemical Physics* **48** 1798 ISSN 00219606 URL <http://scitation.aip.org/content/aip/journal/jcp/48/4/10.1063/1.1668914>
- [34] Schenk M, Seeger T and Leipertz A 2005 *Applied Optics* **44** 6526 ISSN 0003-6935 URL <https://www.osapublishing.org/abstract.cfm?URI=ao-44-31-6526>
- [35] Vestin F, Nilsson K and Bengtsson P E 2008 *Applied Optics* **47** 1893 ISSN 0003-6935 URL <https://www.osapublishing.org/abstract.cfm?URI=ao-47-11-1893>
- [36] van den Bekerom D C M 2018 *To be submitted*
- [37] Long D A 1977 *Raman spectroscopy* (Great Britain: McGraw-Hill) ISBN 0070386757
- [38] Hoskins L C 1975 *Journal of Chemical Education* **52** 568 ISSN 0021-9584 URL <http://pubs.acs.org/doi/abs/10.1021/ed052p568>
- [39] Chedin A 1979 *Journal of Molecular Spectroscopy* **76** 430–491 ISSN 00222852 URL <http://linkinghub.elsevier.com/retrieve/pii/0022285279902364>
- [40] Mantz A, Maillard J P, Roh W B and Narahari Rao K 1975 *Journal of Molecular Spectroscopy* **57** 155–159 ISSN 00222852 URL <http://linkinghub.elsevier.com/retrieve/pii/0022285275900491>
- [41] Creek D M and Nicholls R W 1975 *Proceedings of the Royal Society A: Mathematical, Physical and Engineering Sciences* **341** 517–536 ISSN 1364-5021 URL <http://rspa.royalsocietypublishing.org/cgi/doi/10.1098/rspa.1975.0006>
- [42] Bendtsen J 1974 *Journal of Raman Spectroscopy* **2** 133–145 ISSN 03770486 URL <http://doi.wiley.com/10.1002/jrs.1250020204>
- [43] Penney C M, Peters R L S and Lapp M 1974 *Journal of the Optical Society of America* **64** 712 ISSN 0030-3941 URL <https://www.osapublishing.org/josa/abstract.cfm?uri=josa-64-5-712>
- [44] Bogaard M P, Buckingham a D, Pierens R K and White A H 1978 *Journal of the Chemical Society, Faraday Transactions 1: Physical Chemistry in Condensed Phases* **74** 3008 ISSN 0300-9599 URL <http://xlink.rsc.org/?DOI=f19787403008>
- [45] Altmann K, Strey G, Hochenbleicher J G and Brandmüller J 1972 *Zeitschrift für Naturforschung A* **27** ISSN 1865-7109 URL <https://www.degruyter.com/view/j/zna.1972.27.issue-1/zna-1972-0110/zna-1972-0110.xml>
- [46] Renschler D L, Hunt J L, McCubbin T and Polo S 1969 *Journal of Molecular Spectroscopy* **31** 173–176 ISSN 00222852 URL <http://www.sciencedirect.com/science/article/pii/0022285269903506><http://linkinghub.elsevier.com/retrieve/pii/0022285269903506>
- [47] Cebe J, Giraud M and Smith E 1981 *Chemical Physics Letters* **81** 37–41 ISSN 00092614 URL <http://linkinghub.elsevier.com/retrieve/pii/0009261481853225>
- [48] McDowell R S 1988 *The Journal of Chemical Physics* **88** 356 ISSN 00219606 URL <http://aip.scitation.org/doi/10.1063/1.454608>
- [49] Placzek G and Teller E 1933 *Zeitschrift für Physik* **81** 839–839 ISSN 1434-6001 URL <http://link.springer.com/10.1007/BF01342084>
- [50] Morillo-Candas A S, Klarenaar B L M, Engeln R, Chatterjee A, Booth J P, Silva T, Guerra V and Guaitella O 2017 O atom kinetics in CO₂ pulsed glow discharges *Proceedings of the XXXIII International Conference on Phenomena in Ionized Gases* ed Alves L L and Tejero-del Caz A (Estoril, Portugal: Instituto de Plasmas e Fusão Nuclear, Instituto Superior Técnico, Universidade de Lisboa) p 79 URL http://icpig2017.tecnico.ulisboa.pt/wp-content/uploads/2017/06/ICPIG2017_proceedings.pdf
- [51] Kay J M and Nedderman R M 1974 *An Introduction to Fluid Mechanics and Heat Transfer* 3rd ed (London: Cambridge University Press) ISBN 0521205336 URL <https://www.amazon.co.uk/Introduction-Fluid-Mechanics-Heat-Transfer/dp/0521205336>
- [52] Kentish S E, Scholes C A and Stevens G W 2010 *Recent Patents on Chemical Engineering* **1** 52–66 ISSN 18744788 URL <http://www.benthamdirect.org/pages/content.php?CHENG/2008/00000001/00000001/0005CHENG.SGM>